Journal of Colloid and Interface Science 684 (2025) 552–565

Contents lists available at ScienceDirect

Journal of Colloid And Interface Science

journal homepage: www.elsevier.com/locate/jcis

# Adsorption of $Eu^{3+}$ and $Gd^{3+}$ on high-charge micas as inner-sphere complexes

Marina T. Candela [a,f], Rosa Martín-Rodríguez [b,f], Sofía Díaz-Moreno [c], Rafael Valiente [d,f], Fernando Aguado [e,f,*], Ana C. Perdigón [b,f,**]

[a] Departamento de Biología Molecular, Universidad de Cantabria, Avd. Herrera Oria s/n 39011 Santander, Spain
[b] Departamento QUIPRE, Universidad de Cantabria, Avda. Los Castros 46 39005 Santander, Spain
[c] Diamond Light Source Ltd., Harwell Science and Innovation Campus, Didcot, Oxfordshire OX11 ODE, United Kingdom
[d] Departamento de Física Aplicada, Universidad de Cantabria, Avda. Los Castros 48, 39005 Santander, Spain
[e] Departamento CITIMAC, Universidad de Cantabria, Avda. Los Castros 48, 39005 Santander, Spain
[f] Grupo de Nanomedicina, IDIVAL, Avda. Cardenal Herrera Oria s/n, 39011 Santander, Spain

## HIGHLIGHTS

- Incorporating $RE^{3+}$ cations in high-charge micas occurs in an inner-sphere adsorption mechanism.
- The $RE^{3+}$ ion is located inside the distorted hexagonal cavity, coordinated by 3 oxygens from the tetragonal sheet.
- The tetrahedral layer charge primarily governs the hydration state of $Eu^{3+}$ and $Gd^{3+}$ cations in high-charge mica interlayers.

## GRAPHICAL ABSTRACT

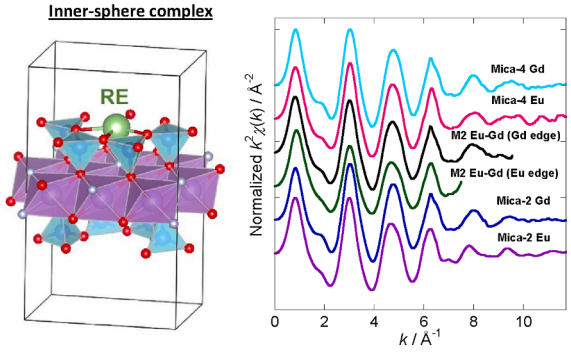


## ARTICLE INFO

*Keywords:*
High-charge micas
Adsorption
EXAFS
Luminescent cations
Europium
Gadolinium

## ABSTRACT

High-charge micas exhibit improved adsorption properties and are a promising alternative clay material for the engineered barrier in deep geological repositories. When combined with $Eu^{3+}$ cations, they serve as an *in situ* luminescent probe for tracking the physical–chemical changes occurring in this engineered barrier over the long term. Therefore, a better understanding of the local environment of the lanthanide is highly desirable to comprehend the specific behavior of these systems. A combination of different techniques, (X-ray diffraction, thermogravimetry, fluorescence, and X-ray absorption spectroscopy), has allowed the study of the local environment of two luminescent lanthanide cations, $Eu^{3+}$ and $Gd^{3+}$ embedded in the galleries of two high-charge

*Abbreviations:* OSC, Outer-sphere complex; ISC, Inner-sphere complex; TG, Thermogravimetry; PXRD, Powder X-ray diffraction; XAS, X-ray absorption spectroscopy; CEC, Cation exchange capacity; RE, Rare Earth; RT, Room Temperature; 2D, Two Dimension; XANES, X-ray absorption near edge structure; EXAFS, Extended X-ray absorption fine structure; CIF, Crystallographic Information File; DTG, Derivative TG; TOT, Tetrahedral and Octahedral; CT, Change Transfer.

* Corresponding authors at: Departamento CITIMAC, Universidad de Cantabria, Avda. Los Castros 48, 39005, Santander, Spain.
** Corresponding authors at: Departamento QUIPRE, Universidad de Cantabria, Avda. Los Castros 46, 39005, Santander, Spain.
*E-mail addresses:* mcd48@alumnos.unican.es (M.T. Candela), rosa.martin@unican.es (R. Martín-Rodríguez), sofia.diaz-moreno@diamond.ac.uk (S. Díaz-Moreno), rafael.valiente@unican.es (R. Valiente), aguadof@unican.es (F. Aguado), perdigonac@unican.es (A.C. Perdigón).

https://doi.org/10.1016/j.jcis.2025.01.015
Received 24 September 2024; Received in revised form 15 December 2024; Accepted 3 January 2025
Available online 4 January 2025

micas with different Si/Al tetrahedral ratio. The results show that the hydration state of these cations is primarily influenced by the layer charge of the aluminosilicate, and secondarily by the cation's hydration enthalpy. High-charge micas doped with trivalent lanthanide cations are more hydrated compared to the original clays with $Na^+$ in the interlayer. Nevertheless, both $Eu^{3+}$ and $Gd^{3+}$ are adsorbed as inner-sphere complexes in the galleries of high-charge micas. They are located inside the distorted hexagonal cavity in all cases, coordinated by 3 oxygens from the tetragonal sheet, one fluorine from the octahedral sheet, and by 2–4 oxygens from water molecules, all at distances around 2.4 Å. An additional oxygen atom at a distance of 3.45–3.50 Å, is proposed from an $H_2O$ molecule in the second coordination shell.

## 1. Introduction

Bentonites are the conventional component of the engineered barrier to retain high-level radioactive waste in deep geological repositories [1,2]. However, other clay materials, particularly high-charge micas, display improved properties and hold great potential for nuclear applications. High-charge micas are synthetic 2:1 phyllosilicates formed by two external tetrahedral sheets of $SiO_4$ and $AlO_4$ that sandwich an octahedral sheet, made of $Mg^{2+}$ complexes. Firstly, these materials have attracted considerable attention because of their unique adsorption properties [3–6]. Specifically, they have a cation exchange capacity of up to 468 meq/100 g, with four negative charges per unit cell. Unlike natural micas, they have hydrated cations located in the interlayer, resulting in better adsorption capacity than bentonites [7–9]. Secondly, high-charge micas, demonstrate greater reactivity for immobilizing radionuclides and exhibit high selectivity for cesium and radium isotope adsorption [10–13]. To study the interaction of radionuclides with clay minerals, including surface adsorption and structure incorporation, lanthanides are used as chemical analogues for trivalent actinides ($Eu^{3+}$ mimic $Am^{3+}$) [14]. Furthermore, the fluorescence features of $Eu^{3+}$ ions offer valuable insights into their local environment and, consequently, into the interaction mechanism between cations and the clay network. Recently, we have developed an *in situ* luminescent probe to track the long-term physical–chemical changes in the clay-engineered barrier under mild hydrothermal conditions. This probe is based on the combination of $Eu^{3+}$ ions and members of the high-charge micas family [10,15]. The emission of $Eu^{3+}$ incorporated into the structure of these aluminosilicates exhibits unique features compared to other layered clays. Specifically, despite the typically forbidden nature of the *f-f* transition, red and green emissions, from the $^5D_0$ and $^5D_1$ excited states of $Eu^{3+}$ to the $^7F_0$ ground state are observed in the luminescence spectra of $Eu^{3+}$ doped sample, contrary to the observation in other layered clays [16]. This behavior depends on the symmetry of the coordination environment of the Eu, which is directly related to both the host structure and the lanthanide cation local environment. Therefore, a better understanding of the local environment of the lanthanide cations embedded in the structure of high-charge micas is highly desirable, as the presence of water molecules near the luminescent ion can provide alternative non-radiative de-excitation pathways. Some studies have been conducted to determine the hydration state of various monovalent, divalent, and trivalent cations in the interlayer space of high-charge micas [17,18]. However, to our knowledge, no studies have been conducted to determine the location of luminescent cations and their hydration state in the bi-dimensional galleries of those aluminosilicates [16].

The ability of the interlayer cations to adsorb water is responsible for the expansion of the clay and its adsorption capacity, thus modulating its optical properties [19]. Therefore, considering that the primary adsorption mechanism described for high-charge micas is via ion-exchange reaction, analyzing the local environment of the interlayer cation and its hydration state are fundamental issues, particularly relevant for environmental applications. So, the hydration state of the interlayer cation is highly influenced by the 2D confinement effect of the clay sheets under electrostatic interaction. Hence, the ability of an ion to hydrate is the result of different factors, mainly the nature of the interlayer cation (valence, radius, hydration enthalpy) and the clay layer charge (value and origin either from the tetrahedral or the octahedral sheet) [20]. Depending on the mentioned parameters, cations incorporated in the interlayer can form either outer-sphere complexes (OSC) or inner-sphere complexes (ISC) [21]. An ISC, which is partially hydrated, can bind with the basal oxygens of the tetrahedral layer. In contrast, an OSC, being fully hydrated, retains at least one water molecule between the cation and the clay surface. Pavón *et al.* determined that, in these high-charge micas, the number of water molecules per cation in a series of metal ions is proportional to the cation charge and ionic radius ratio ($q/r$) [17]. Under this premise, the hydration capacity for cations with low $q/r$ values is limited, so an ISC configuration would be expected. On the contrary, for cations with larger $q/r$ values, more water molecules can be incorporated into the interlayer space of micas, making the formation of an OSC a possibility that cannot be fully ruled out.

Here, we present an in-depth study of the local environment of two luminescent lanthanide cations, namely $Eu^{3+}$ and $Gd^{3+}$, embedded in the galleries of two high-charge micas, with 2 and 4 charges per unit cell, using a combination of different techniques. Both cations, are characterized by a high electrostatic parameter, suggesting a significant degree of solvation, with an OSC configuration expected. However, this configuration shows low compatibility with the luminescent features observed on the Eu-doped samples, as previously described. To analyze the influence of the electric field from the silicate layer on the formation of either OSC or ISC, two micas were selected based on different Si/Al ratios in the tetrahedral layer. For this purpose, a suitable combination of long- and short-range order techniques has been used to shed light on the local environment of the luminescent cations. Thermogravimetry (TG) measurements and the interlayer distance, calculated from Powder X-ray diffraction (PXRD), will provide information about the water content in the galleries. In addition, the number of water molecules directly coordinated to the cation will be inferred from luminescence lifetime values. Furthermore, the *b lattice* parameter will be used to evaluate the distortion of the hexagonal cavity of the tetrahedral layer. The coordination number and the local structure of the interlayer cation will be evaluated using X-ray absorption spectroscopy (XAS).

## 2. Materials and Methods

### 2.1. Synthesis of high-charge micas

High-charge micas with 2 (Mica-2) and 4 (Mica-4) charges per unit cell, having the chemical composition $Na_nMg_6Si_{8-n}Al_nO_{20}F_4$, (where $n = 2, 4$), were synthesized following the method described by Park *et. al.* [8]. Stoichiometric powder amounts of $SiO_2$, $Al(OH)_3$ and $MgF_2$, and an excess of NaCl were mixed by grinding and allowed to react in a Pt crucible at 900 °C for 15 h. After cooling, the samples were washed with deionized water to eliminate any soluble impurities and dried at 65 °C or room temperature. The specific surface area values of Mica-2 and Mica-4 are 4 $m^2/g$ [22].

### 2.2. Cation exchange reaction

Mica-2, with a theoretical cation exchange capacity (CEC) of 234 meq·100 $g^{-1}$, and Mica-4, with a CEC of 468 meq·100 $g^{-1}$, were

subjected to an aqueous ion exchange reaction with $Eu^{3+}$ and/or $Gd^{3+}$ cations [23]. Typically, 300 mg of clay were dispersed in a 50 ml solution of deionized water containing europium and/or gadolinium nitrates and stirred for 24 h. The amount of $RE(NO_3)_3$, was chosen in such a way that the CEC becomes 2.5 times that of the clay. Subsequently, the samples were centrifuged four times at 5000 r.p.m. for 15 min each. This process was repeated three more times to ensure a satisfactory degree of incorporation of the RE ions in the clay. Finally, the samples were washed with deionized water for 24 h, centrifuged again, and dried in air at 60 °C for 24 h.

### 2.3. Characterization

PXRD. PXRD experiments were performed in a Bruker D8 Advanced diffractometer equipped with a Cu tube as the x-ray source and a Lynxeye 1D detector. Measurements were taken in the 3-70° (2$\theta$) range and the resulting diffraction patterns were analyzed with TOPAS software. TG. TG analysis was performed on a Setaram Setsys evolution TGA/DSC model. The sample was heated from room temperature (RT) to 800 °C at a heating rate of 10 °C·min$^{-1}$ in air. Approximately 20 mg of the sample was heated in an open platinum crucible. Spectroscopy. All spectroscopic measurements were carried out using samples in powder form. Emission, excitation, and lifetime measurements were performed using a FLSP920 spectrofluorometer from Edinburgh Instrument, equipped with double monochromators and different excitation sources (a continuous-wave 450 W Xe lamp and a pulsed 60 W Xe lamp). The luminescence was detected with an electrically cooled photomultiplier tube R928P (Hamamatsu, Shizuoka, Japan). XAS. XAS measurements, including XANES and EXAFS regions, were carried out at the Diamond Light Source synchrotron (beamline I20-Scanning) [24]. Experiments were performed in transmission mode, exploring the $L_{III}$-edge of Eu (6977 eV) or Gd (7243 eV). For XAS measurements, pellets of 13 mm diameter were made by mixing cellulose and powder of the mica under study, in such a way that the amount of sample corresponds to a thickness of three absorption lengths. XAS measurements were taken in three different positions of the pellet and three times at each position and after that, they were merged to obtain an average spectrum. The processing and analysis of the EXAFS data were performed with Athena and Artemis software [25], respectively, while the XANES region was analyzed qualitatively.

## 3. Results and Discussion

Fig. 1 shows the PXRD patterns and Pawley fitting of the as-synthesized Mica-2 and Mica-4. Characteristic basal and structural reflections of the mica-type phase are present in the pattern of both samples. Patterns can be described as a function of the following three families of reflections. The first family of peaks can be associated with a mica phase structure with hydrated $Na^+$ ions in the interlayer space of the clay. The second family of reflections (indicated by "b" in Fig. 1) is also ascribed to the mica phase with dehydrated $Na^+$ cations between layers. Finally, traces of a magnesium silicate called forsterite, $Mg_2SiO_4$ (JPDS no. 34–0189), have also been identified, in agreement with previous reports [26]. For the as-synthesized high-charge micas, PXRD patterns have been indexed assuming a monoclinic symmetry. The lattice parameters are included in Table 1.

Fig. 2 compares the most intense (001) reflection for the as-synthesized high-charge micas and the exchanged samples. PXRD patterns of the sample with the highest layer charge with hydrated sodium in the interlayer (Mica-4) show a basal spacing of 12.10 Å. A similar value of 12.26 Å has been obtained for the high-charge mica with the lowest layer charge (Mica-2). This finding is compatible with a single monolayer of water in the interlayer space of both micas. Interestingly, the main basal reflections (001) of the samples exchanged with lanthanide ions shift towards lower 2θ angles, to ~ 6.5° in Mica-4 and to ~ 5.9° in Mica-2, resulting in a higher basal spacing of the phyllosilicate,

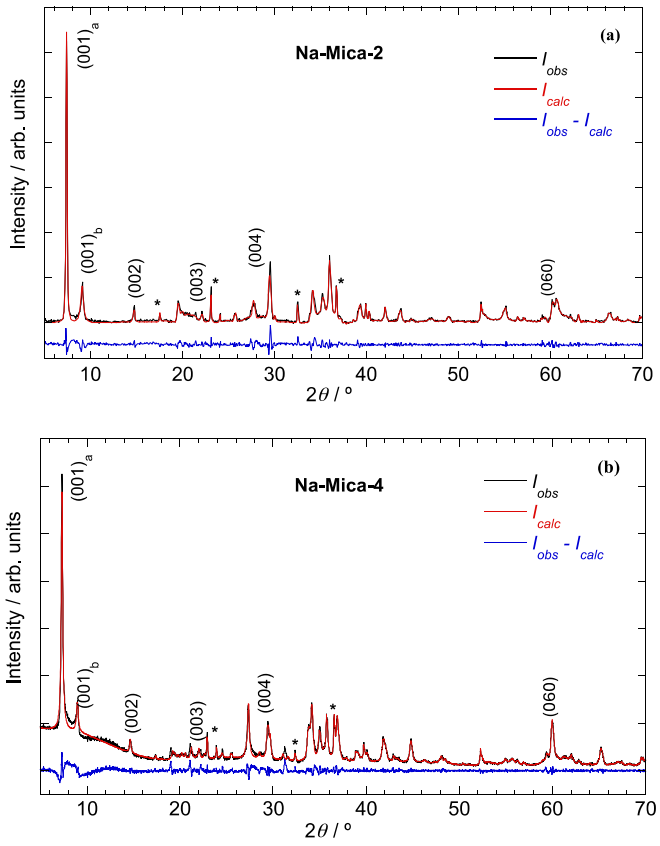


**Fig. 1.** PXRD patterns of the as-synthesized Mica-2 (a) and Mica-4 (b). Pawley fit between experimental (black) and calculated (red) lines. The main (00*l*) basal reflections and the (060) reflection are indicated in both patterns. *: The asterisks indicate the peaks corresponding to traces of the forsterite impurity phase. (For interpretation of the references to colour in this figure legend, the reader is referred to the web version of this article.)

**Table 1**
Lattice parameters (*a*, *b*, *c*, *β*) of the most hydrated phase of high-charge micas before and after the cation-exchange reaction. The basal space ($d_{001}$) of all clays is also shown, together with the position of its diffraction peak. Uncertainties are shown in parenthesis.

| Sample | *a* / Å | *b* / Å | *c* / Å | *β* / Å | $d_{001}$ / Å | 2*θ* / ° |
|---|---|---|---|---|---|---|
| Mica-2 | 5.315(1) | 9.247 (2) | 12.38(2) | 98.1(9) | 12.26 | 7.21 |
| Mica-2 Eu | 5.319*[a] | 9.236*[a] | 15.1152 (8) | 97.86 (8) | 14.97 | 5.90 |
| Mica-2 Gd | 5.315* | 9.247* | 15.08(8) | 99.21 (3) | 14.87 | 5.94 |
| Mica-2 Eu-Gd | 5.315* | 9.247* | 15.061(3) | 97.89 (3) | 14.92 | 5.92 |
| Mica-4 | 5.3223 (8) | 9.248 (2) | 12.27(5) | 99.4 (1.4) | 12.10 | 7.30 |
| Mica-4 Eu | 5.327*[a] | 9.253*[a] | 13.654(2) | 98.81 (2) | 13.49 | 6.55 |
| Mica-4 Gd | 5.3223* | 9.248* | 13.692(1) | 98.60 (2) | 13.54 | 6.53 |

* Fixed value. [a] Small differences in *a* and *b* lattice parameters of RE-Mica-*n* arise from distinct synthesis batches, leading to separate refinements.

$d_{001} \approx 13.5$ Å in Mica-4 and $d_{001} \approx 15$ Å in Mica-2. The increase in the basal spacing can be attributed to the incorporation of more hydrated rare-earth ions in the interlayer space, which causes the swelling of the clay. It is well known that the tendency of the interlayer counterions to solvate is responsible for the clay expansion in the presence of water

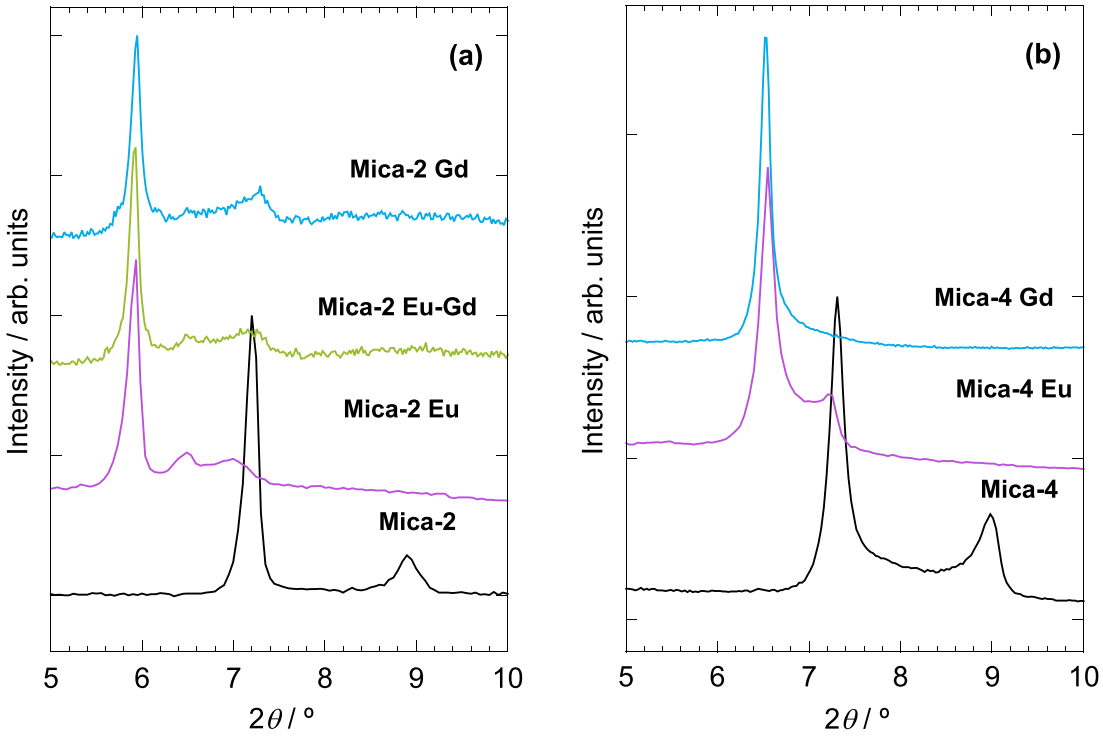


**Fig. 2.** (001) reflection of the as-synthesized and exchanged Mica-2 (a) and Mica-4 (b).

[20]. Thus, the *q/r ratio* is a fundamental parameter in determining the hydration capacity of the cation, as can be inferred from the hydration enthalpy values included in Table 2.

In a first approximation, an ion's tendency to be incorporated in the form of either an ISC or OSC in swelling clays can be deduced based on its ability to hydrate. For instance, $Na^+$ tends to form a solvation shell of six water molecules and has a hydration enthalpy of −406 kJ/mol. Under this weak solvation effect, a second parameter comes into play: the origin of the layer charge, whether from octahedral or tetrahedral substitution. In swelling clays with tetrahedral isomorphic substitution, the charge is more localized, and $Na^+$ ions tend to form an ISC within the confined 2D interlayer space. In contrast, when the charge arises from isomorphic substitution in the octahedral sheet, it is more shielded, and $Na^+$ ions adopt an OSC conformation [20]. In this case, the sodium ion is less tightly bound to the layer, as the shielding effect from the octahedral substitution reduces the ion's direct interaction with the charged surface. According to this rule, sodium in high-charge micas where up to four negative layer charges are from the isomorphic substitution of silicon by aluminum in the tetrahedral layer- would favor the ISC conformation, due to the more localized charge and greater interaction with $Na^+$. In line with this, Kalo *et al.* report that sodium cations are coordinated to three basal oxygen atoms of the tetrahedral sheet and three oxygen atoms of intercalated water in a sodium brittle mica [27].

As shown in Fig. 2, the (001) reflection for the exchanged samples with trivalent cations is located at lower 2$\theta$ angles, suggesting that more water molecules are adsorbed, leading to a higher basal distance. It is well known that the extent of water adsorption increases with hydration enthalpy, so a more hydrated state is expected for $Eu^{3+}$ and $Gd^{3+}$ cations, which have similar hydration enthalpies, (−3535 kJ/mol, and −3545 kJ/mol, respectively) compared to $Na^+$ (−406 kJ/mol) [28]. It has to be mentioned, that cations with a high solvation enthalpy (ex. $Ca^{2+}$ $\Delta H = -1560$ kJ/mol) tend to form OSC in swelling clays [29]. Specifically, the exchange of Mica-2 and Mica-4 with the smaller cation $Al^{3+}$ (0.53 Å), with a value of hydration enthalpy of −4460 kJ/mol, has resulted in a most hydrated interlayer space, with basal spacing about 14.0 Å and 13.5 Å, respectively [17].

Additionally, after the incorporation of the lanthanide cations in the bi-dimensional galleries of both micas (Fig. 2), the clay's expansion is larger in Mica-2 than in Mica-4. This behavior can be explained by the fact that the solvation of lanthanides confined within the clay sheets is influenced not only by the *q/r* ratio and the hydration energy of the interlayer cation but also by the charge of the clay. In the case of Mica-4, four tetrahedral silicon atoms per unit cell are isomorphically substituted by aluminum ions, whereas in the case of Mica-2, only two are substituted. Thus, the net negative charge of Mica-4 is higher than that of Mica-2. Consequently, the basal spacing is smaller in the former case due to the greater electrostatic interaction between the layer and the positively charged interlayer cations. Finally, traces of less hydrated mica phases after the cation exchange reaction can also be observed in the PXRD pattern of the exchanged samples. Table 2 summarizes the lattice parameters of the most hydrated phase of the different high-charge micas, as well as the estimated basal distance.

According to the position of the (060) reflection in the PXRD patterns, the degree of distortion of the silica tetrahedra has also been analyzed for Mica-2 and Mica-4. The (060) reflections are located at approximately 60° (2θ) in both cases, with a $d_{060}$ distance of about 1.54 Å, which is typical for trioctahedral clays [32]. The $SiO_4$ tetrahedra in the tetrahedral layer of the clay are interconnected and form hexagonal rings with varying degrees of distortion. This deformation arises from the opposite rotation of adjacent $SiO_4$ tetrahedra in the (001) plane. It is assumed that the rotation of the tetrahedral is due to the size misfit between the tetrahedral and octahedral layers, as the former is larger

**Table 2**
Physicochemical properties of cations.

| | $Na^+$ | $Eu^{3+}$ | $Gd^{3+}$ |
|---|---|---|---|
| $r$ (Å)[a] | 1.02 | 0.95 | 0.94 |
| $q/r$ | 0.98 | 3.17 | 3.20 |
| $\Delta H°_{hydr}$ (kJ/mol) | −406 | −3535 | −3545 |

[a] Sixfold coordination ionic radii [30]. *q/r*: cation charge and ionic radius relation. $\Delta H°_{hydr}$ is the molar hydration enthalpy [31].

than the latter [18,33]. Classically, an estimation of the average rotation ($\alpha$), *i.e.* the average deviation from 120° has been evaluated through the following expression: $\cos(\alpha) = b_{obs} / b_{theor}$, where $b_{obs}$ is the observed lattice parameter (Table 3) and $b_{theor}$ represents the ideal lattice parameter. Parameter $b_{theor}$ depends on the theoretical degree of isomorphic substitution of $Si^{4+}$ ions in the tetrahedral sheet by $Al^{3+}$ ones and can be approximated as $b_{theor}$ ($Si_{1-x}Al_x$) = 9.15 Å + 0.74$x$ [18]. The average rotation or tilt angle can vary from a few degrees up to a maximum of 30°, corresponding to the situation in which basal oxygens of the tetrahedral sheet point to the center of the hexagonal cavity (Fig. 3).

Based on the values collected in Table 3, Mica-4, the synthetic clay with the highest layer charge, shows the largest estimated distortion angle ($\alpha$ = 13.7°), consistent with previous results [18]. A distorted hexagonal cavity has been related to the difficulty for the clay to swell, so a lower hydration state is expected in the interlayer space of Mica-4 compared to Mica-2. Brigatti *et al.* reported that large $\alpha$ values correspond to small interlayer separation [34]. Assuming the models proposed by Hazen *et al.* [35] and by Kalo *et al.* [27], the smallest values of the tilt angle have been found from the crystal structure of a natural mica with two negative layer charges ($\alpha$ = 5.8° if calculated from the Crystallographic Information File (CIF), or α = 8.6° from the expression $\cos(\alpha) = b_{obs} / b_{theor}$). This value increases if a synthetic mica with four negative layer charges is considered, up to $\alpha$ = 12.0° calculated from the CIF structure file, or to 13.7° from the expression $\cos(\alpha) = b_{obs} / b_{theor}$. These values are not far from the estimates in this work $\alpha$ = 7.8° for Mica-2 and $\alpha$ = 13.7° for Mica-4. In any case, a most distorted hexagonal cavity has been found for the mica with the highest layer charge.

The hydration state of both micas as a function of the physical chemistry parameters of the interlayer cations has been monitored using TG analysis. Fig. 4 displays the TG curves of the starting and exchanged samples with $Eu^{3+}$ and $Gd^{3+}$ cations. Typically for clay minerals, the main mass loss step in the thermogram occurs below 400 °C, primarily due to water evaporation. This includes the loss of interlayer water and water associated with the silicate network. The number of mass loss steps and their temperatures are related to the physicochemical properties of the cation and the layer charge of the silicate. Mica-2 and Mica-4 with $Na^+$ as interlayer cation exhibit a single mass loss step of approximately 5 % and 6 % below 250 °C, respectively. This is associated with the evaporation of hydration water molecules of the interlayer cation and the evaporation of water from the clay surface. The observed mass loss allows estimation of the number of water molecules per $Na^+$ ion, approximately 1.2 for Mica-2 and 0.7 for Mica-4. These numbers of water molecules are evidently insufficient to complete the hydration sphere of $Na^+$ cations in the interlayer, supporting the hypothesis that sodium cations adopt an inner-sphere complex configuration in tetrahedrally charged aluminosilicates [20]. These results are in agreement with those previously reported [17].

Additionally, the layer charge of the silicate directly influences the hydration state of $Na^+$, reducing the electrostatic parameter and consequently decreasing the cation's hydration capacity. In contrast to sodium micas, the mass loss curves of $Eu^{3+}$ and $Gd^{3+}$ exchanged samples exhibit multiple steps, suggesting the presence of diverse water molecules bound to the clay structure with varying strengths. Specifically, new mass loss steps are observed at higher temperatures, ~ 210 °C in Mica-2 and ~ 165 °C in Mica-4. Table 4 presents the onset temperatures of the derivative TG (DTG) water evaporation peak, weight loss of the process, number of water molecules per unit cell, and number of water molecules per cation from TG. A complete replacement of the interlayer cation has been considered.

**Table 3**
Observed and theoretical lattice parameter $b$ ($b_{obs}$ and $b_{theor}$, respectively) along with the estimated tilt angle (α) from them.

| Sample | $b_{obs}$ / A | $b_{theor}$ / Å | $\alpha$ / Å |
|---|---|---|---|
| Mica-2 | 9.247(2) | 9.335 | 7.8375 |
| Mica-4 | 9.2484(15) | 9.52 | 13.7190 |

The mass loss due to water evaporation in the exchanged samples is significantly higher, ranging from ~ 8.5 % to ~ 10.6 %, compared to the original samples. In a preliminary analysis, the hydration energy of the interlayer cations ($Eu^{3+}$ and $Gd^{3+}$) acts as the primary driving force controlling the solvation rate, being directly proportional to the electrostatic parameter ($q$ /$r$).

The number of water molecules per $Eu^{3+}$ and $Gd^{3+}$ estimated from this mass loss is 8.3 and 6.6 in Mica-2, respectively. However, these numbers decrease to 3.0 and 2.5 water molecules when considering only the most strongly bound water (corresponding to the second mass loss peak, from 150 °C to 300 °C). In Mica-4, the number of water molecules per $Eu^{3+}$ and $Gd^{3+}$ is reduced to 4.0 and 4.8, respectively, with only 1.4 associated with the second mass loss of water. These results indicate that the hydration state of the clay is influenced by two main factors: the hydration enthalpy of the interlayer cation and the value of the tetrahedral layer charge. The estimated number of water molecules per interlayer cation decreases as the layer charge increases. Detailed TG results are summarized in Table 4.

A complementary study of the conformation and hydration state of the cation in the interlayer space of high-charge micas has been conducted using spectroscopic measurements. Firstly, the normalized RT emission and excitation spectra of $Eu^{3+}$ exchanged clays are shown in Fig. 5. The excitation spectra were recorded while detecting emission at 609 or 614 nm, whereas the emission spectra were measured under 393 nm excitation. The excitation spectra of $Eu^{3+}$ consist of four groups of narrow peaks corresponding to *f-f* transitions from the $^7F_0$ ground state to different excited states. In the case of Mica-2 Eu-Gd, a broad band centered around 280 nm can be observed, which is associated with an $O^{2-} \rightarrow Eu^{3+}$ charge transfer (CT) band. It suggests that the $Eu^{3+}$ ions are coordinated with basal oxygens [16]. A less intense band can also be observed in Mica-2 Eu and Mica-4 Eu spectra.

To obtain structural information using $Eu^{3+}$ as a local luminescent probe, we focused primarily on four particular features: (i) The absence or presence of emission peaks corresponding to the $^5D_1 \rightarrow {}^7F_0$ transition (green emission); (ii) The nature of emission peaks corresponding to the $^5D_0 \rightarrow {}^7F_0$ transition; (iii) The splitting of the $^5D_0 \rightarrow {}^7F_1$ transition and (iv) The integrated intensity ratio between magnetic dipole $^5D_0 \rightarrow {}^7F_1$ and electric dipole $^5D_0 \rightarrow {}^7F_2$ transitions. Firstly, the presence of $Eu^{3+}$ luminescence from the $^5D_1$ excited state in high-charge micas confirms the low phonon energy of the clay (preventing, thus, multiphonon relaxation processes), as well as the fact that the $Eu^{3+}$ are not aggregated but homogeneously distributed (hence decreasing cross-relaxation processes). Besides, the appearance of the $^5D_1$ green emission supports the idea that $Eu^{3+}$ is in the interlayer space of the aluminosilicates, as proposed in previous studies [16]. Regarding the second point, it should be remembered that only sites with $C_s$, $C_n$, or $C_{nv}$ symmetry will give rise to an observable peak corresponding to the $^5D_0 \rightarrow {}^7F_0$ transition since $J = 0 \rightarrow J' = 0$ transition is strictly forbidden according to the standard Judd-Offelt theory. This transition can be used for the determination of the presence of non-equivalent crystallographic sites in the host lattice. The spectral region of the $Eu^{3+}$ luminescence corresponding to this transition shows an asymmetric broad peak for all the studied clays. High-resolution $Eu^{3+}$ photoluminescence measurements on this spectral range allow us to observe at least two distinct contributions to this peak in the case of high-charge micas, as a consequence, the presence of at least two slightly different local environments for the $Eu^{3+}$ ions in the interlayer cannot be fully discharged. In addition, the energy of this transition has been reported to be sensitive to the surroundings of the luminescent ion [36]. In the case of the gas phase (free ion), the energy position of the $Eu^{3+}$ $^5D_0$ level is placed at 17374 $cm^{-1}$, while for hydrated $Eu^{3+}$ ions ($Eu^{3+}{\cdot}9H_2O$) it is usually found to range between 17277 and 17280 $cm^{-1}$ [36,37]. In general, the position of this transition is found to redshift as a result of the chemical bonding, making this shift more noticeable for $Eu^{3+}$ located in crystalline host materials [36].

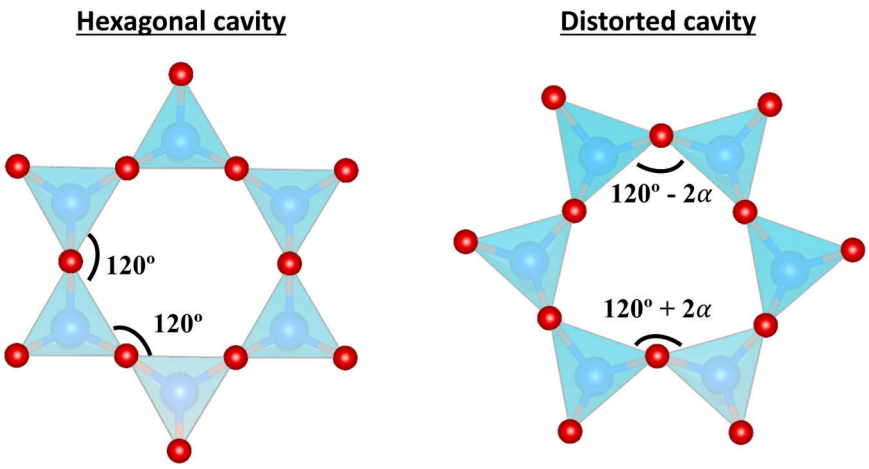


**Fig. 3.** Scheme showing a perfect hexagonal cavity (left) and a distorted hexagonal cavity (right) due to the tetrahedra rotation by an angle $\alpha$.

In our case, the $^5D_0$ level is centered around 17300 $cm^{-1}$ in all cases (Table 5), in accordance with $Eu^{3+}$ in a partially hydrated state.

Point (iii) is related to the spectral shape of the $^5D_0 \rightarrow {}^7F_1$ emission band. This transition, magnetic dipole in origin, reflects the crystal filed splitting of the $^7F_1$ level and provides information about $Eu^{3+}$ ions environment. Specifically, the total removal of crystal field degeneracy results in three sublevels for $^7F_1$. The fact that more than three peaks are observed suggests the presence of more than one coordination environment for $Eu^{3+}$ ions. Finally, and related to the point (iv), the ratio ($R$) between the integrated intensities of $^5D_0 \rightarrow {}^7F_2$ (hypersensitive) and $^5D_0 \rightarrow {}^7F_1$ transitions is usually used as a measure of the site inversion center of $Eu^{3+}$ ions. In the case of the studied $Eu^{3+}$ exchanged clays, $R$ is found to range between 2.6 and 2.8, as shown in Table 5. This indicates that $Eu^{3+}$ ions are located at sites with relatively small distortions. Besides, the similarity of $R$ for both Mica-2 and Mica-4 suggests that the adsorption mechanisms could be similar throughout the clay series. In any case, this hypothesis must be taken with care, since the second coordination sphere of $Eu^{3+}$ ions can have an impact on the $Eu^{3+}$ photoluminescence spectra, and therefore, in the asymmetry ratio $R$ [38].

The decay curves of $Eu^{3+}$ in selected clays are shown in Fig. 6. The decay in Mica-2 Eu was fitted to a single exponential ($Ae^{-t/\tau}$) while the decay curves of $Eu^{3+}$ in Mica-2 Eu-Gd and Mica-4 Eu had to be fitted to a double exponential ($Ae^{-t/\tau 1} + Be^{-t/\tau 2}$). This fact suggests that in Mica-2 all $Eu^{3+}$ ions are located in the interlayer space surrounded by the same number of water molecules. On the contrary, lifetime measurements in co-doped Mica-2 and Mica-4 imply that $Eu^{3+}$ ions with different hydrated state coexist. The obtained photoluminescence lifetimes have been also included in Table 5.

The $Eu^{3+}$ luminescence lifetime can be related to the number of water molecules ($n_{H_2O}$) surrounding the luminescent ion [36]. Lifetimes are usually shorter for $RE^{3+}$ ions in aqueous media due to energy transfer processes from their excited 4$f$ levels ($^5D_0$ level in case of $Eu^{3+}$) to non-radiative multiphonon relaxation processes involving water molecules. Several empirical laws have been proposed to estimate the hydration state of distinct $RE^{3+}$ or actinide ions, including $Eu^{3+}$, $Cm^{3+}$, or $Am^{3+}$ [36]. In the case of $Eu^{3+}$, the number of water molecules in the first coordination sphere can be estimated by Eq. (1), where the lifetime must be in ms:

$$n_{H_2O}(Eu^{3+}) = \frac{1.07}{\tau(ms)} - 0.62 \quad (1)$$

In the case of Mica-2 Eu, the fluorescence lifetime can be related to the presence of 3.7 water molecules around the $Eu^{3+}$ ion, which is in agreement with the ~ 3 water molecules obtained by TG measurements, in accordance with our previous study [16]. For Mica-2 Eu-Gd and Mica-4 Eu, if only the longer lifetime is taken into account; the estimated number of water molecules directly coordinated to the ion is 2.4 and 1.4, as summarized in Table 5, in agreement with TG results and the distorting angle obtained by PXRD. Those data corroborate the low hydration state of the cation in all the studied samples pointing out the formation of an ISC. However, the second (shorter) lifetimes detected in Mica-2 Eu-Gd and Mica-4 Eu indicate the coexistence of $Eu^{3+}$ cations in a different hydrated state, the number of water molecules being 5.4 for Mica-2 Eu-Gd and 4.2 for Mica-4 Eu.

Fig. 7 shows the excitation (a) and emission (b) spectra of $Gd^{3+}$ ions in high-charge $n$-micas ($n$ = 2 and 4). The excitation spectra of $Gd^{3+}$ ions, measured by recording the emission at 311 nm, consist of two groups of narrow peaks originated by transitions from the $^8S_{7/2}$ ground state to $^6D_J$ and $^6I_J$ excited states. On the other hand, the emission spectra of $Gd^{3+}$ ions are characterized by two sharp line emission bands from $^6P_{5/2} \rightarrow {}^8S_{7/2}$ ($\lambda \sim 305$ nm) and $^6P_{5/2} \rightarrow {}^8S_{7/2}$ ($\lambda \sim 311$ nm) optical transitions. It has been observed that the emission intensity of the sample with $Gd^{3+}$ ions decreases in the order $I_{\text{Mica-2}} > I_{\text{Mica-4}} > I_{\text{Mica-2 Eu-Gd}}$.

The temporal evolution of the $^6P_{7/2} \rightarrow {}^8S_{7/2}$ $Gd^{3+}$ luminescence has been measured by detecting the emission at 311 nm after short-pulsed excitation at 272 nm. The decay curves (Fig. 8) have been fitted in all cases to a single exponential, indicating a homogeneous local environment around the interlayer cation, and the $Gd^{3+}$ emission lifetimes were found to be 5.3, 5.1 and 3.5 ms for Mica-2 Gd, Mica-4 Gd, and Mica-2 Eu-Gd, respectively.

XAS measurements (including both X-ray absorption near edge structure (XANES) and extended X-ray absorption fine structure (EXAFS) regions) have been performed to obtain information about the local environment of the exchanged $Eu^{3+}$ and $Gd^{3+}$ ions, aiming to elucidate their position, oxidation state, and coordination number ($N$) within the clays. The XANES region of the spectra for $Eu^{3+}$ and $Gd^{3+}$ exchanged clays are shown in Fig. S1, together with that of C-type $Eu_2O_3$ and $Gd_2O_3$, which have been employed as standards..The white line peak position in C-type $Eu_2O_3$ and europium exchanged clays is located around 6983.3 eV, which allows us to corroborate that europium ions are indeed in the trivalent oxidation state (as inferred by the optical properties). In the case of Gd-exchanged clays, the white line peaks are in the same position as in C-type $Gd_2O_3$, this is, at 7249.1 eV, which indicates that $Gd^{3+}$ is the dominant oxidation state. There is no pre-peak before the absorption edge in any of the XANES spectra, indicating that both $Eu^{3+}$ and $Gd^{3+}$ ions are located in a high-symmetry environment and probably coordinated by a large number of atoms. Lanthanide atoms are usually found in seven to nine-fold coordination [39]. The XANES signal of all $Eu^{3+}$ or $Gd^{3+}$ exchanged clays and the standards are similar (with the only exception of the oscillation band that appears after the absorption edge, which is found at higher energies in the case of the standards), suggesting that the coordination environments could be

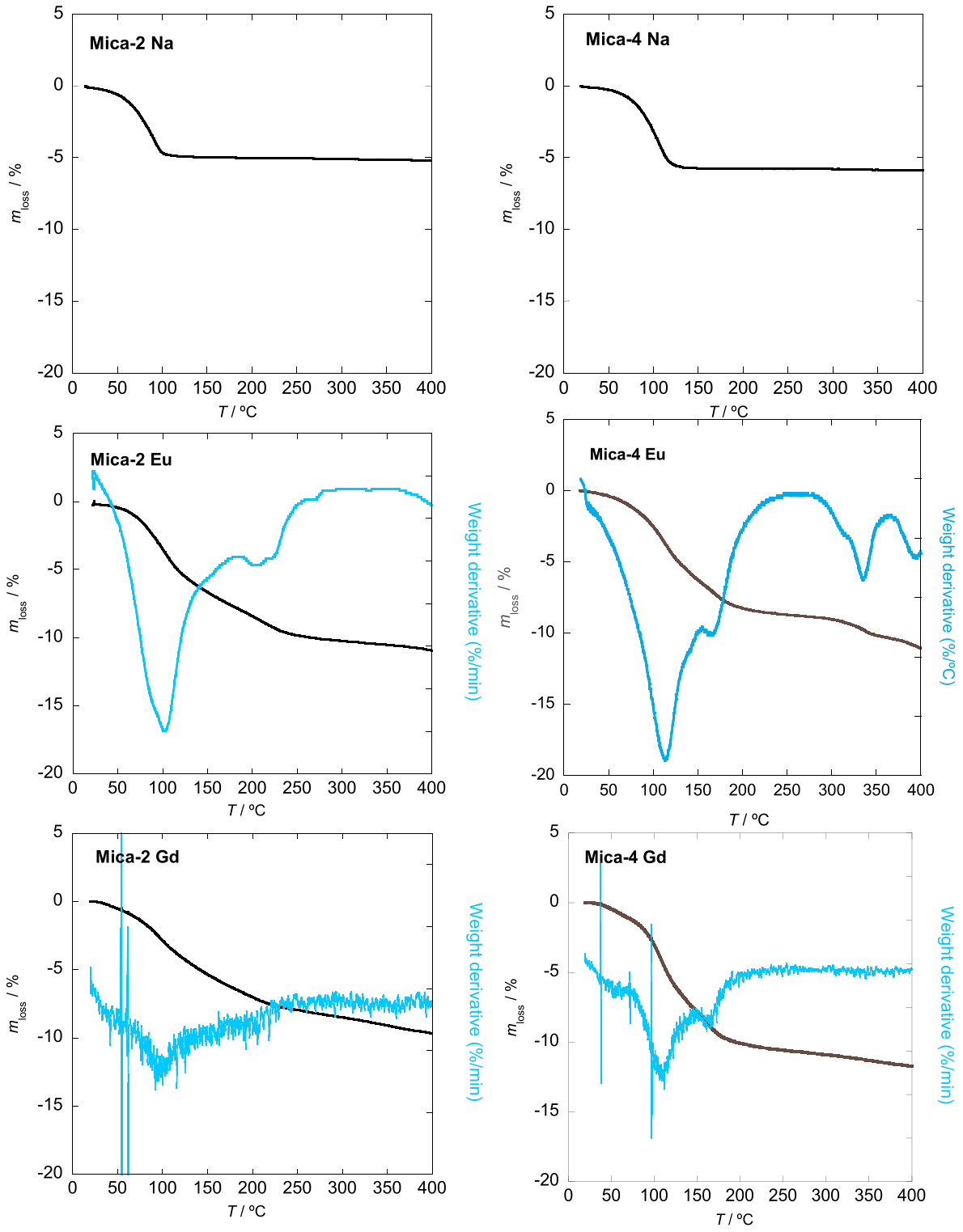


**Fig. 4.** TG and DTG curves of Mica-2 (left) and Mica-4 (right) samples exchanged with different cations.

comparable in all cases. This result might indicate an analogous first coordination sphere to the employed standards, where the $RE^{3+}$ ions are six-fold coordinated by oxygen anions at an average distance of 2.30 Å for $Gd_2O_3$ and 2.33 Å for $Eu_2O_3$.

To carry out the EXAFS analysis, and due to the high correlation between the amplitude reduction factor ($S_0^2$) and $N$ (which can lead to large uncertainties in the latter parameter, up to 10–20 %), the value of $S_0^2$ was calculated from the standards C-type $Eu_2O_3$ (s.g. *Ia*-3, a = 10.882 (2) Å) and C-type $Gd_2O_3$ (s.g. *Ia*-3, a = 10.8211(2) Å). The obtained values were $S_0^2 = 1.09 \pm 0.12$ for $Eu_2O_3$ and $S_0^2 = 1.07 \pm 0.12$ for $Gd_2O_3$ (see fits and details about the fitting procedure in Supplementary Information, Figs. S2 and S3 and Tables S1 and S2) and they were fixed in the subsequent EXAFS analysis of $Eu^{3+}$ and $Gd^{3+}$ exchanged clays, respectively. EXAFS spectra of the RE-exchanged clays in the *k*-space and *R*-space are included in the Supplementary Information (Fig. S4). Several structural models for the $RE^{3+}$ incorporation have been

**Table 4**
Onset temperatures of the DTG water evaporation peak, weight loss of the process, number of water molecules per unit cell, and number of water molecules per cation from TG. Number of water molecules calculated between 150 °C and 300 °C inside the brackets.

| Sample | *T* / °C | % weight loss | $H_2O$ molec./u.c. | $H_2O$ molec./cation |
|---|---|---|---|---|
| Mica 2 | | | | |
| $Na^+$ | 80 | 5.0 | 2.39 | 1.20 |
| $Eu^{3+}$ | 101 213 | 9.9 | 5.58 | 8.30 (3.0) |
| $Gd^{3+}$ | 100 206 | 8.50 | 4.34 | 6.60 (2.5) |
| Mica 4 | | | | |
| $Na^+$ | 100 | 5.7 | 2.90 | 0.73 |
| $Eu^{3+}$ | 116 167 | 9.0 | 5.26 | 3.95 (1.4) |
| $Gd^{3+}$ | 111 165 | 10.6 | 6.41 | 4.81 (1.4) |

considered in an attempt to explain the different contributions observed in the EXAFS spectra of the $RE^{3+}$ exchanged clays and they are depicted in Fig. 9. These models reflect the three possible retention mechanisms: i) the RE ions are incorporated in the clay structure (Fig. 9a), ii) they form outer-sphere complexes (Fig. 9(b)), iii) they form inner-sphere complexes (Fig. 9c and d). The clay structures proposed by Hazen *et al.* (s.g. *C*2/*m*) [35] and by Kalo *et al.* (s.g. *C*2) [27] have been used as a starting model for Mica-2 and Mica-4, respectively.

The first model (N1) considers that the $RE^{3+}$ ion is incorporated in the octahedral layer, substituting a $Mg^{2+}$ ion (Fig. 9a). Thus, its first coordination sphere would be formed by 4 oxygen (O) and 2 fluor (F) anions at an average distance of ~ 2.07 Å (according to the initial model). To account for the size mismatch between the ionic radii of $Mg^{2+}$ (0.72 Å, six-fold) and $Eu^{3+}$ (0.947 Å) or $Gd^{3+}$ ions (0.938 Å), the change in the interatomic distance parameter ($\Delta r$) has been set in the range 0.22–0.25 Å during the fitting process, in such a way that no more distortions than necessary were produced in the tetrahedral and octahedral layers (TOT). Fig. S5 shows an example of the fit obtained for the first shell of Mica-2 Gd according to this model. The corresponding derived parameters are summarized in Table S3. The fit does not account for the first contribution of the EXAFS spectra even considering the size mismatch, evidencing thus the incorrectness of this model to describe the $Gd^{3+}$ incorporation mechanism. Since the first contribution in the EXAFS spectra of all $Eu^{3+}$ and $Gd^{3+}$ exchanged clays is centered around the same position as in Mica-2 Gd, this $RE^{3+}$ incorporation model can be also ruled out for all of them. Indeed, the incorporation of $RE^{3+}$ ions in the octahedral sheet seems rather unfavorable due to the size mismatch between the original and substituting ions, which would necessarily lead to large distortions in the TOT layers and broader peaks in the PXRD pattern (opposed to what it has been observed). However, it must be noted that it has been proposed as the possible retention mechanism of $Fe^{3+}$ and $Y^{3+}$ ions in Montmorillonite and hectorite clays, respectively [40,41]. Besides, this model has been proposed for the $Lu^{3+}$ ions uptake by the precursor phase of hectorite, brucite [42]. At the same time, the incorporation of $RE^{3+}$ ions in the tetrahedral sheet has not been considered either, due to the larger size mismatch between $Si^{4+}$ and $RE^{3+}$ ions and the low coordination number ($N = 4$).

The second model (N2) accounts for the incorporation of the $RE^{3+}$ ions in the interlayer space, forming outer-sphere complexes. Several authors have reported the existence of outer-sphere complexes combined with inner-sphere complexes in several RE ions ($Cs^+$ and $La^{3+}$) adsorbed on vermiculite and montmorillonite [43,44]. Here, two variants have been considered: i) the $RE^{3+}$ ion is in the middle of the interlayer space (N2.1), and ii) the $RE^{3+}$ ion is in the interlayer space but not necessarily in the middle of it, but closer to the upper or lower tetrahedral sheets although not interacting with them (N2.2). Regarding model N2.1, if only the clay's structure is considered (*i.e.*, no water molecules), the first neighbors in high-charge micas would be the basal oxygens from the hexagonal cavities in the upper and lower tetrahedral sheets. Nonetheless, these oxygen atoms are too far away to account for the first, second, and almost even third contribution observed in the

**Table 5**
Position of the emission band corresponding to the $^5D_0 \rightarrow {}^7F_0$ transition (in nm and $cm^{-1}$), together with the asymmetry intensity ratio *R* ($^5D_0 \rightarrow {}^7F_2$ / $^5D_0 \rightarrow {}^7F_1$) and the $Eu^{3+}$ fluorescence lifetimes ($\tau_1$, $\tau_2$) of Mica-*n* Eu ($n = 2,4$) and Mica-2 Eu-Gd clays. The number of water molecules estimated through Eq. (1) and the longer lifetime ($\tau_1$) are also included.

| Sample | $\lambda_{^5D_0 \rightarrow {}^7F_0}$ (*nm*) | $\lambda_{^5D_0 \rightarrow {}^7F_0}$ ($cm^{-1}$) | *R* | $\tau_1$ (μs) | $n_{H_2O}$(±0.5) | $\tau_2$ (μs) |
|---|---|---|---|---|---|---|
| Mica-2 Eu | 577.6 | 17313 | 2.6 | 250 | 3.7 | – |
| Mica-2 Eu-Gd | 577.9 | 17304 | 2.7 | 352 | 2.4 | 179.5 |
| Mica-4 Eu | 577.9 | 17304 | 2.8 | 543 | 1.4 | 221 |

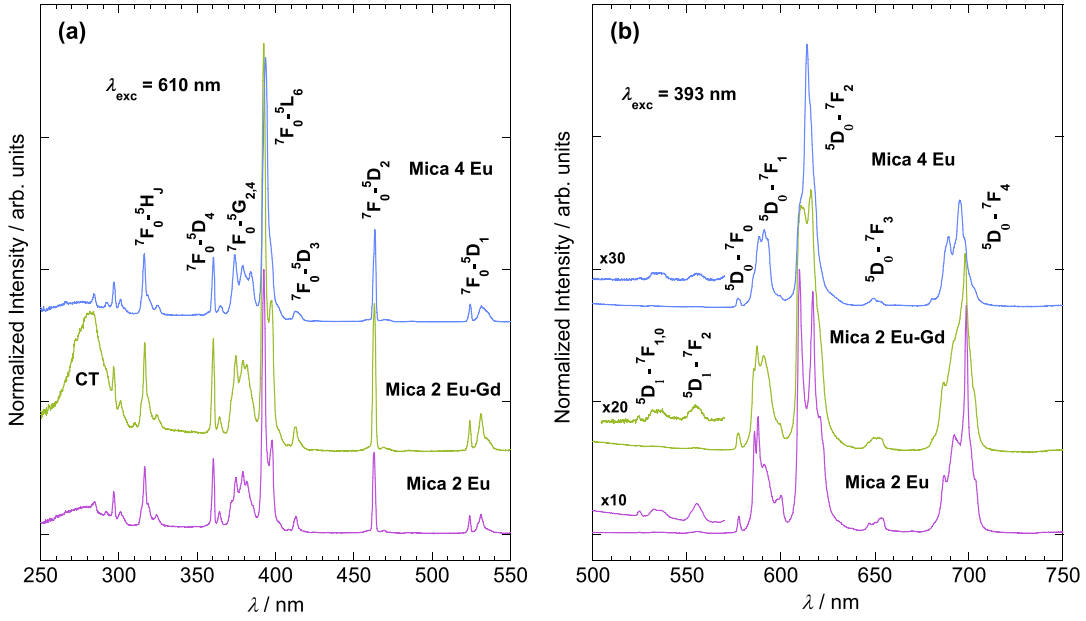


**Fig. 5.** RT excitation spectra detecting $^5D_0$ emission at 610 nm (a) and emission spectra upon excitation at 393 nm (b) of $Eu^{3+}$ ions in several high-charge micas.

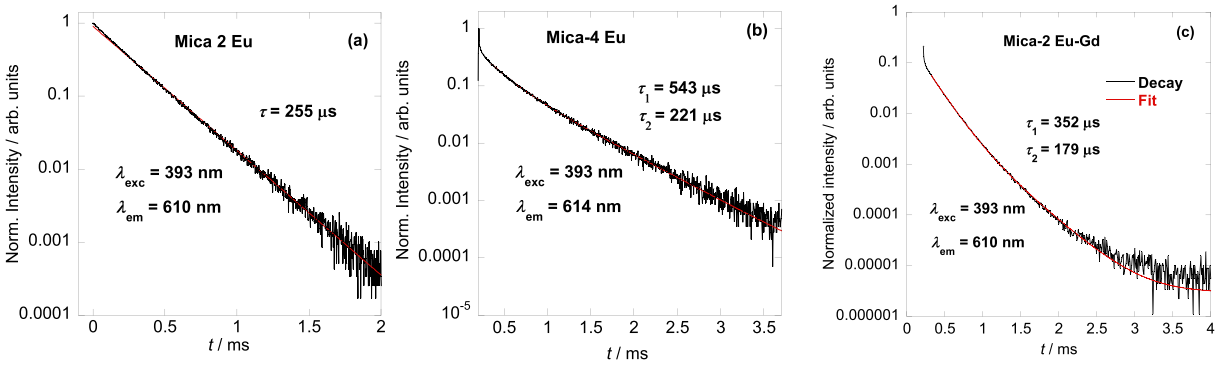


**Fig. 6.** Decay curves of the $^5D_0 \rightarrow {}^7F_2$ $Eu^{3+}$ emission intensity in selected clays: (a) Mica-2 Eu, (b) Mica-4 Eu, and(c) Mica-2 Eu-Gd. They were measured under 393 nm excitation and detecting at 609 or 614 nm.

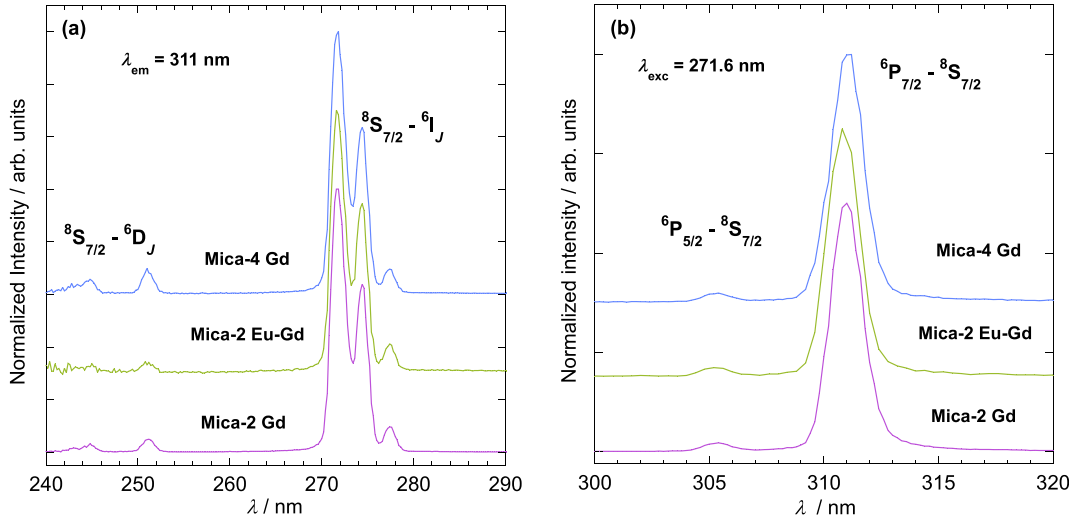


**Fig. 7.** RT excitation spectra detecting $^6P_{7/2}$ emission at 311 nm (a) and emission spectra upon excitation at 271.6 nm (b) of $Gd^{3+}$ ions in several high-charge micas.

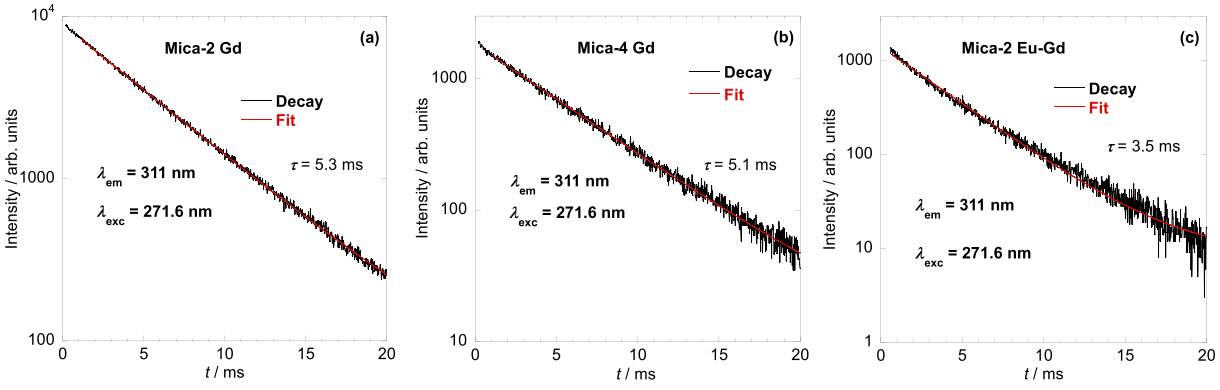


**Fig. 8.** Decay curves of the $^6P_{7/2} \rightarrow {}^8S_{7/2}$ $Gd^{3+}$ luminescence in selected clays: (a) Mica-2 Eu, (b) Mica-4 Eu, and(c) Mica-2 Eu-Gd. They were measured under 311 nm excitation and detecting at 271.6 nm.

EXAFS spectra of Mica-2 RE (Hazen's structural model [35]). Differently, they could be part of the second and third shells observed in the EXAFS spectra of Mica-4 RE (Kalo's structural model [27]). This is related to the lower basal space and the shift of the upper and lower tetrahedral sheets in the latter clays, which brings the oxygens closer to the RE ion (see Tables S4 and S5 for representative distances in Mica-2 and Mica-4 according to the structural models employed). Thus, the unexplained contributions of this model would need to be due to oxygen atoms from surrounding water molecules. On the assumption that the first and second contributions of the EXAFS spectra are due to oxygen ions (in this case, mostly from water molecules), the coordination number of the $RE^{3+}$ ion (either $Gd^{3+}$ or $Eu^{3+}$) would be $N \sim 7$–8 at distances between 2.40–2.42 Å for the first shell, and $N \sim 3$ at distances $\sim 3.5$ Å for the second shell, according to the EXAFS fitting (see Fig. 10 for a fitting example of Mica-2 Gd, Mica-2 Eu and Mica-4 Gd). Table 6 summarizes the fit values of the parameters refined during the fitting of the first and second shells of the EXAFS data ($N$, $r_{RE\text{-}O}$, $\sigma^2$) assuming both contributions are due to oxygen scatterers from water molecules (model

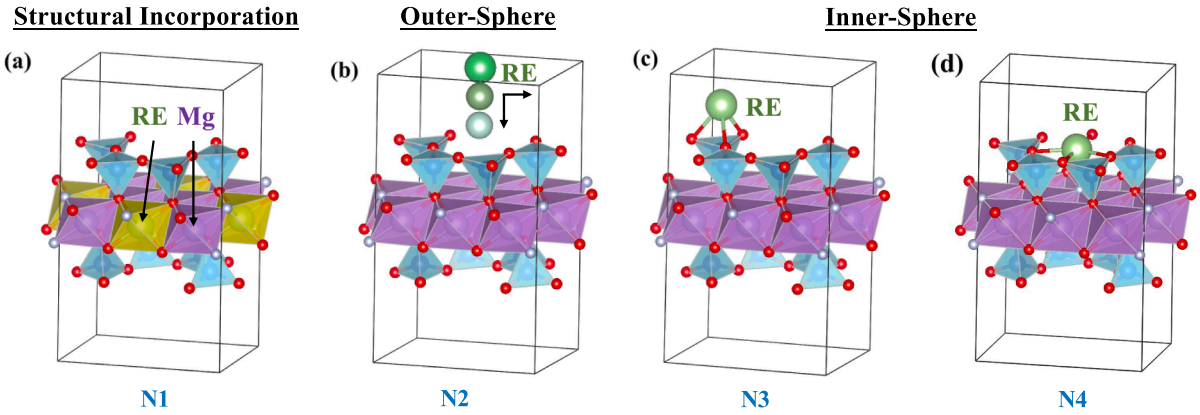


**Fig. 9.** Scheme of the different retention mechanisms that have been evaluated, which correspond to (a) the incorporation of the RE ion in the structure (model N1), (b) the RE ion in an outer-sphere complexation (model N2, later subdivided in N2.1 and N2.2) and (c,d) the RE ion acting as an ISC (models N3 and N4). Note that in model N2, the three atoms in different shades of green are just a guide to the eye representing different possible positions/heights of the RE ion within the interlayer space. (For interpretation of the references to colour in this figure legend, the reader is referred to the web version of this article.)

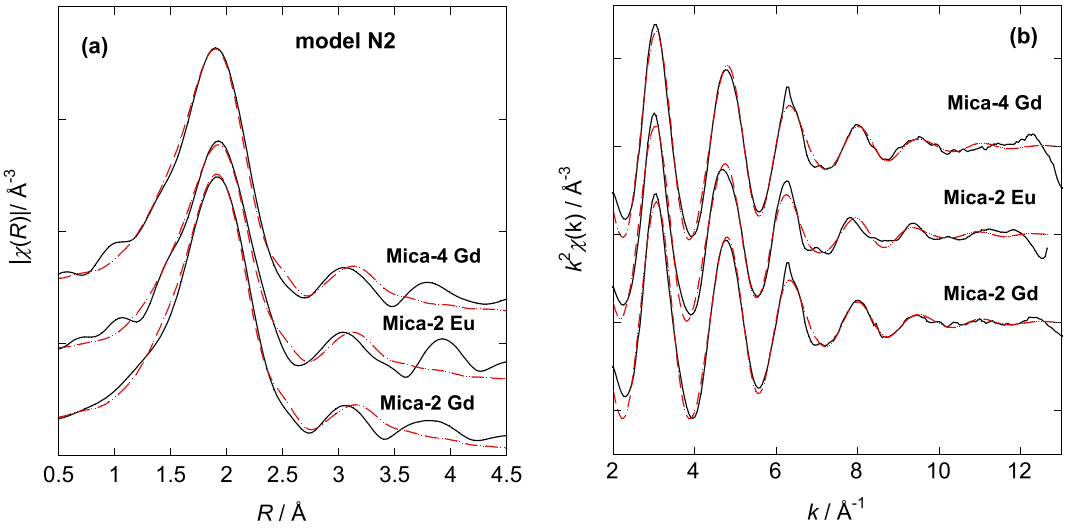


**Fig. 10.** EXAFS spectra (black solid line) and fitting (red dotted line) in *R*-space (a) and *k*-space (b) of RE-exchanged Mica-*n* (RE = Eu, Gd, $n = 2, 4$) according to model N2.1 and up to the second shell. (For interpretation of the references to colour in this figure legend, the reader is referred to the web version of this article.)

N2.1). Note that in the case of Mica-2 Eu-Gd, only the first shell was analyzed, since the available *k*-range was too short due to the interference with Gd $L_{III}$ or Eu $L_{II}$ edges (7243 eV and 7617 eV, respectively), depending on whether Eu or Gd edges were being explored, respectively.

As just mentioned, in the case of Mica-2 RE-exchanged clays (RE = Eu, Gd) the third contribution that can be distinguished in the EXAFS spectra cannot be explained by the oxygen scatterers from the tetrahedral sheet either, since they are still too far apart (4.6–4.9 Å), which allows to discard this retention mechanism for these clays (as a shortening of these RE-O distances would imply a reduction in the basal space, in contradiction with the XRD results). In the case of Mica-4 RE, with a lower basal distance, the presence of an oxygen anion from the tetrahedral sheet at ~ 3.4 Å may explain part of the second contribution of the EXAFS spectra and also, oxygens located further away (4.0 and 4.25 Å) could contribute to the third shell. However, it must be noted that according to the previous results (Table 6), at least ~ 7–10 $H_2O$ molecules would be needed in the interlayer space of the exchanged micas to account for model N2.1. This would be in contradiction with the TG results, from which a lower number of water molecules has been derived. Thus, it seems highly unlikely that model N2.1 accounts for the incorporation of the $Eu^{3+}$ (or $Gd^{3+}$) in any of the studied high-charge micas. Regarding model N2.2, it considers that the second shell would be due to oxygens belonging to the tetrahedral sheet, but the first one would still be due to oxygens from presumably water molecules. Since the number of first neighbors was calculated to be about 7–8, this would not be in accordance again with the number of most bounded water molecules estimated by TG either. Therefore, the incorporation of the RE ions as OSC can also be ruled out. Given these results, the retention mechanism of $Eu^{3+}$ and $Gd^{3+}$ ions in these high-charge micas should be, therefore, as ISC.

Two different models (N3 and N4) have been evaluated to account for possible retention mechanisms as inner-sphere complexes. Model N3 (Fig. 9c) considers the $RE^{3+}$ ion is located above one of the tetrahedra of the distorted hexagonal cavity of the tetrahedral sheet and coordinated by three basal oxygens and 3–5 water molecules at an average distance of ~ 2.39–2.42 Å (as obtained from the analysis of the first coordination shell in the previous model (Table 6)). Also, according to the fixed model, a Si atom would be present at ~ 2.5 Å. The next nearest neighbors would be 3Si atoms at ~ 3.9 Å, which seem to be a bit further away to be responsible for the second contribution of the EXAFS spectra as corroborated after the fitting procedure (see as an example the fit of Mica-4 Gd in Fig. S6 and Table S6). Note that the poor fit of the second shell suggests that this model probably does not explain the retention mechanism of the $RE^{3+}$ ions.

**Table 6**
Best fit values of the parameters refined during the fitting of the first and second shells of the EXAFS data ($N$, $r_{RE\text{-}O}$, $\sigma^2$) assuming both contributions are due to oxygen scatterers from water molecules (model N2.1). Parameters corresponding to the first and second coordination spheres appear with the subscripts 1 and 2, respectively. In the case of Mica-2 Eu-Gd, the second shell was not fitted due to the short $k$-range available. Parameters with a superscript "f" indicate that the values were fixed during the fit. During the fitting of the second shell, the values of $N$, $r$, and $\sigma$ from the first shell were fixed.

| Sample | $k$-range | $N_1$ | $r_{RE\text{-}O1}$ / Å | $\sigma_1^2$ / Å$^2$ | $N_2$ | $r_{RE\text{-}O2}$ / Å | $\sigma_2^2$ / Å$^2$ |
|---|---|---|---|---|---|---|---|
| Mica-2 Gd | 2.7–11.3 | 8.3 (6) | 2.400 (10) | 0.013 (2) | 3.5 (1.5) | 3.52(2) | 0.013 (9) |
| Mica-2 Eu | 2.7–11.7 | 7.2 (7) | 2.424 (12) | 0.013 (2) | 3.0 (1.4) | 3.52(2) | 0.011 (8) |
| Mica-2 Eu-Gd (Gd edge) | 2.7–7.7 | 8.5 (5) | 2.408 (17) | 0.013$^f$ | – | – | – |
| Mica-2 Eu-Gd (Eu edge) | 2.7–6.7 | 7.4 (6) | 2.420$^f$ | 0.013$^f$ | – | – | – |
| Mica 4 Gd | 2.7–11.3 | 7.9 (6) | 2.396 (10) | 0.013 (2) | 3.9 (1.7) | 3.52(2) | 0.013 (8) |
| Mica 4 Eu | 2.7–10.7 | 7.3 (5) | 2.408 (11) | 0.012 (2) | 3(2) | 3.53(3) | 0.01(1) |

On the other hand, model N4 (Fig. 9d) considers that the RE ion is located inside the distorted hexagonal cavity, in such a way that it is coordinated by 3 oxygens from the tetragonal sheet, one F from the octahedral sheet (indistinguishable from an O during the EXAFS analysis) and 2–4 oxygens from water molecules, all of them at distances around 2.4 Å. The next nearest neighbors would be O, Si, or Mg atoms located at 2.7–3.7 Å (see bond lengths in Tables S7 and S8). Fig. 11 (a,b) shows representative fitted EXAFS spectra of Mica-2 and Mica-4 RE-exchanged clays up to the second shell according to this model, and, Table S9 summarizes the parameters and paths used in the fit. Note that during the fitting procedure, the $\Delta r$ parameter has been set again to $\Delta r = 0$ for all paths, except the RE-O and RE-Si ones at ~ 2.40 Å and ~ 3.15 Å, respectively, which have been refined, as they were averaged paths. From Fig. 11(a and b) it can be observed that model N4 can explain to some extent the second contribution observed in the EXAFS spectra of the majority of the micas, although not completely.

So far, the possibility that the second contribution observed in the spectra is influenced by the presence of oxygens from further water molecules has not been considered during the analysis (except models N2.1 or N2.2). However, two "jumps" were observed in the TG curves of $RE^{3+}$ exchanged micas, which were ascribed to water molecules linked

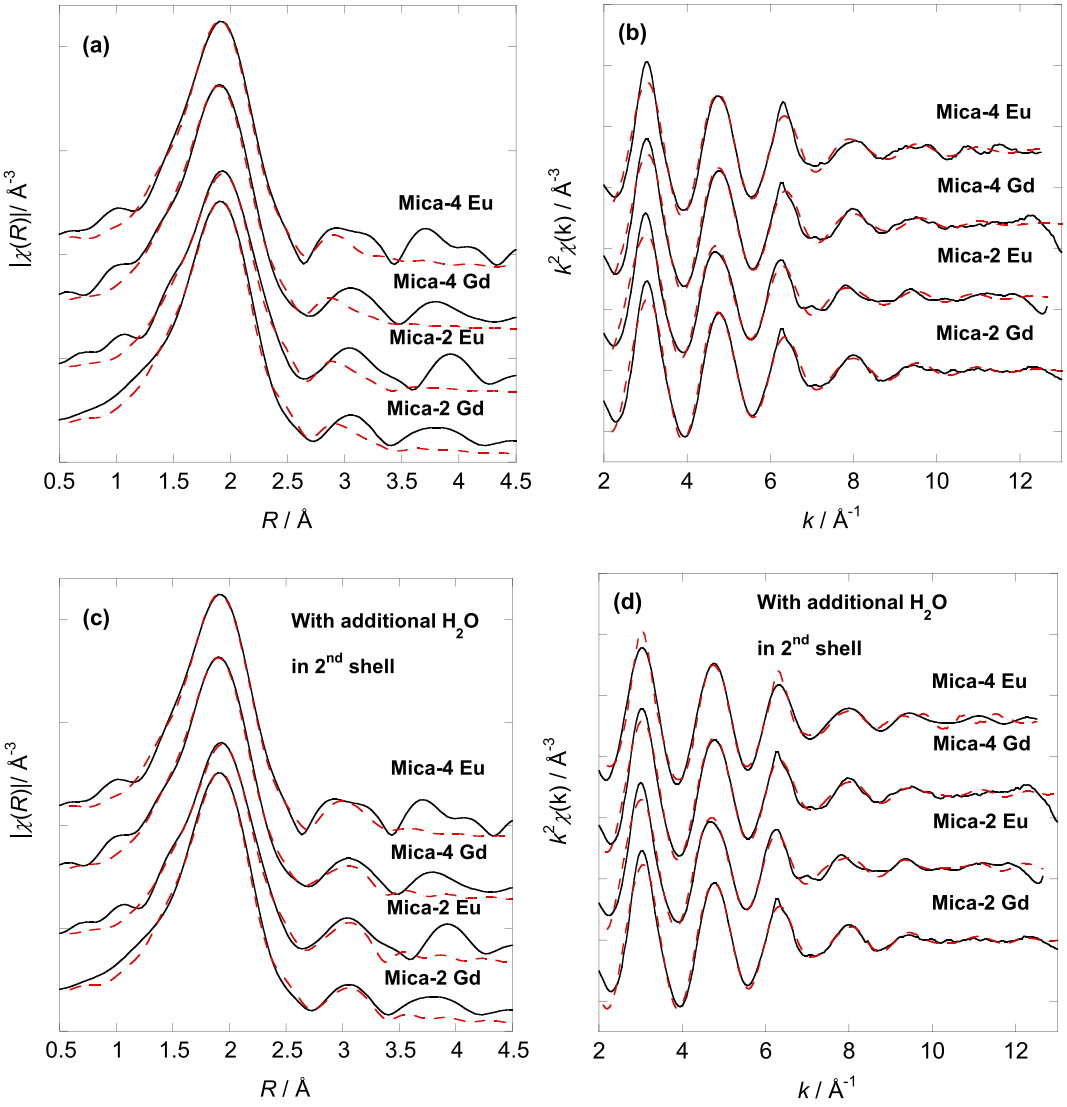


**Fig. 11.** EXAFS spectra (black solid line) and fitting (red dotted line) in $R$- and $k$-space of RE-exchanged Mica-$n$ (RE = Eu, Gd, $n$ = 2, 4) according to model N4 and up to the second shell. The fits in (c, d) correspond to those in which an additional oxygen from a distant water molecule has been included during the fitting of the second shell, while those in (a, b) correspond to those in which it has not. (For interpretation of the references to colour in this figure legend, the reader is referred to the web version of this article.)

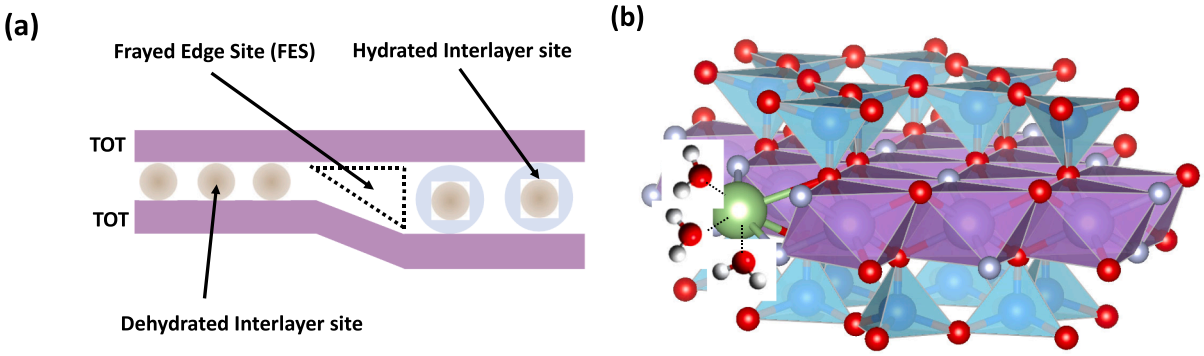


**Fig. 12.** (a) Scheme visualizing the frayed edge sites. (b) Structural model of the incorporation of the RE ion on the edge of the clay's platelets.

with different strengths. To take into account this possibility, an additional RE-O path simulating an $H_2O$ molecule was included during the fitting process of the second shell, and the resulting fits are shown in Fig. 11(c and d). Table S10 includes the parameters derived from the fitting of the first and second shells of the EXAFS spectra of Mica-*n* RE (*n* = 2,4 and RE = Eu. Gd) according to model N4 plus one additional oxygen in the second shell. It can be seen that the addition of this new oxygen atom, which would be at a distance of 3.45–3.50 Å, notably improves the quality of the fit in all cases. It must be mentioned that an alternative model derived from N4, in which the $RE^{3+}$ ion is placed in the hexagonal cavity of the tetrahedral sheet but somewhat off-centered and at a certain height ($h \sim 0.6$–$0.7$ Å), in such a way that it is coordinated by three basal oxygens at ~ 2.40 Å, has also been studied. Notwithstanding, the fittings did not match the EXAFS data properly and it was not further considered. Thus, considering all investigated models, N4 seems to be the one that better describes the observed EXAFS data.

Several considerations must be contemplated when looking at the results obtained through the EXAFS analysis. Firstly, to carry out the fittings, we have used a structural model adapted from that proposed by Hazen [35] or by Kalo *et al.* [27]. However, the degree of distortion of the hexagonal cavity in our clays could be somewhat different from that described by them, and that could lead to slightly distinct results since the absorber-scatterer atom distances beyond the first shell would be modified, which makes it more difficult to find the exact location of the $RE^{3+}$ ion within the clay (although it seems with the most probability that the RE ions act as ISC). Secondly, we have assumed that the environment of the trivalent lanthanide is always the same. Nonetheless, slightly different sites were inferred through luminescence measurements of the $Eu^{3+}$ ions in both Mica-2 and Mica-4, and thus, a weighted average is observed through EXAFS. Also, within the group of models representing inner-sphere adsorption, there are two that have not been considered here but have been reported to explain the retention mechanism of some ions in distinct clays. The first one is the incorporation of the exchanged ions in the denominated "frayed edge sites". A frayed edge site can be defined as the intermediate wedge-shaped area that exists between a hydrated and non-hydrated interlayer, as schemed in Fig. 12a.

This retention mechanism has been proposed to explain the initial incorporation of Cs ions in the interlayer space of illite clays [45]. Secondly, the incorporation of the $RE^{3+}$ ions can also occur on the edges of the clay platelets, in such a way that they would share corners with the Si tetrahedra and edges with the Mg octahedra, as schemed in Fig. 12b. This has been proposed as the possible mechanism for $Y^{3+}$ in hectorite [46] or for U in montmorillonite [47]. Nonetheless, if that was the principal incorporation mechanism of the studied $RE^{3+}$ ions in this work, that would not require the expansion of the basal space that we have observed through XRD experiments, which might suggest that it is not the main retention mechanism either (although the existence of a fraction of $RE^{3+}$ ions incorporated in this way, or in any other way, cannot be excluded).

## 4. Conclusions

The present work reports the location of the luminescent cations $Eu^{3+}$ and $Gd^{3+}$ and their hydration state in the bi-dimensional galleries of high-charge micas. Depending on the clay layer charge and the cation hydration enthalpy, cations in the interlayer of clays can form either OSC or ISC conformations. According to the results presented here, the incorporation of the two $RE^{3+}$ cations in high-charge micas occurs through an inner-sphere adsorption mechanism, despite their high water content, as revealed by TG and PXRD measurements. Therefore, the tetrahedral layer charge is the key parameter controlling the hydration state of both cations in the interlayer of high-charge micas. In the exchanged samples, the water molecules directly coordinated to the cation are insufficient to fully complete their coordination sphere, resulting in a partially hydrated state. The $RE^{3+}$ ion is located inside the distorted hexagonal cavity, coordinated by 3 oxygens from the tetragonal sheet, one F from the octahedral sheet, and 2–4 oxygens from water molecules, all of them at distances around 2.4 Å. The next nearest neighbors would be O, Si, or Mg atoms located at 2.7–3.7 Å. This conclusion is also supported by the number of water molecules calculated from the fluorescence lifetime of the $^5D_0 \rightarrow {}^7F_2$ $Eu^{3+}$ emission intensity of $Eu^{3+}$.

## CRediT authorship contribution statement

**Marina T. Candela:** Writing – original draft, Methodology, Investigation, Formal analysis, Data curation. **Rosa Martín-Rodríguez:** Writing – review & editing, Supervision, Funding acquisition, Data curation, Conceptualization. **Sofía Díaz-Moreno:** Validation, Formal analysis, Data curation. **Rafael Valiente:** Validation, Investigation. **Fernando Aguado:** Writing – review & editing, Supervision, Methodology, Investigation, Formal analysis, Data curation, Conceptualization. **Ana C. Perdigón:** Writing – review & editing, Supervision, Funding acquisition, Conceptualization.

## Declaration of competing interest

The authors declare the following financial interests/personal relationships which may be considered as potential competing interests: Ana C. Perdigon, Rosa Martin Rodriguez, Fernando Aguado and Rafael Valiente have patent #WO 2021/224534 A1. Other authors declare that they have no known competing financial interests or personal relationships that could have appeared to influence the work reported in this paper.

## Acknowledgment

This work has been supported by the Spanish Ministerio de Ciencia e Innovación, Project ref. TED2021-131305B-I00 financed by MCIN/ AEI /10.13039/501100011033 and by the European Union-

NextGenerationEU/PRTR. We would like to thank IDIVAL, Project INNVAL19/18 for financial support. M. T. Candela acknowledges the predoctoral grant "Concepción Arenal" (University of Cantabria- Government of Cantabria). The authors thank Diamond Light Source for beamtime (proposal SP19223-1) and financial support and the I20-Scanning beamline staff for all the assistance received.

## Appendix A. Supplementary data

Supplementary data to this article can be found online at https://doi.org/10.1016/j.jcis.2025.01.015.

## Data availability

Data will be made available on request.

## References

[1] R. Zuo, Z. Xu, X. Wang, J. Yang, X. Du, C. Du, W. Cai, Y. Xu, Z. Wu, Adsorption characteristics of strontium by bentonite colloids acting on claystone of candidate high-level radioactive waste geological disposal sites, Environ Res 213 (2022) 113633, https://doi.org/10.1016/j.envres.2022.113633.

[2] M. Xie, D. Su, K.U. Mayer, K.T.B. MacQuarrie, Reactive transport investigations of the long-term geochemical evolution of a multibarrier system including bentonite, low-alkali concrete and host rock, Appl. Geochem. 143 (2022) 105385, https://doi.org/10.1016/j.apgeochem.2022.105385.

[3] Y.D. Noh, S. Komarneni, K.J.D. MacKenzie, H.M. Ro, M. Park, Highly charged swelling micas of different charge densities: Synthesis, characterization, and selectivity for Sr and Ba, Sep Purif Technol 104 (2013) 238–245, https://doi.org/10.1016/j.seppur.2012.11.028.

[4] R. Ravella, S. Komarneni, Synthesis of swelling micas with stoichiometric amount of fluorine, characterization and ion exchange studies, Appl Clay Sci 39 (2008) 180–185, https://doi.org/10.1016/j.clay.2007.05.009.

[5] F.J. Osuna, E. Pavón, M.D. Alba, $Pb^{2+}$, $Cd^{2+}$ and $Hg^{2+}$ removal by designed functionalized swelling high-charged micas, Sci. Total Environ. 764 (2021) 142811, https://doi.org/10.1016/j.scitotenv.2020.142811.

[6] F.J. Osuna, E. Pavón, M.D. Alba, Design swelling micas: Insights on heavy metals cation exchange reaction, Appl Clay Sci 182 (2019) 105298, https://doi.org/10.1016/j.clay.2019.105298.

[7] S. Komarneni, R. Pidugu, J.E. Amonette, Synthesis of Na-4-mica from metakaolinite and MgO: Characterization and $Sr^{2+}$ uptake kinetics, J Mater Chem 8 (1998) 205–208, https://doi.org/10.1039/a706050e.

[8] M. Park, D.H. Lee, C.L. Choi, S.S. Kim, K.S. Kim, J. Choi, Pure Na-4-mica: Synthesis and characterization, Chem. Mater. 14 (2002) 2582–2589, https://doi.org/10.1021/cm0116267.

[9] M.D. Alba, M.A. Castro, M. Naranjo, E. Pavón, Hydrothermal reactivity of Na-n-micas (n = 2, 3, 4), Chem. Mater. 18 (2006) 2867–2872, https://doi.org/10.1021/cm0514802.

[10] R. Martín-Rodríguez, F. Aguado, M.D. Alba, R. Valiente, E. Pavón, A.C. Perdigón, Exploring the local environment of the engineered nanoclay Mica-4 under hydrothermal conditions using $Eu^{3+}$ as a luminescent probe, J Alloys Compd 921 (2022) 166086, https://doi.org/10.1016/j.jallcom.2022.166086.

[11] M. José García-Jiménez, A. Cota, F.J. Osuna, E. Pavón, M.D. Alba, Influence of temperature and time on the $Eu^{3+}$ reaction with synthetic Na-Mica-n (n=2 and 4), Chemical Engineering Journal 284 (2016) 1174–1183, https://doi.org/10.1016/j.cej.2015.09.077.

[12] F.J. Osuna, A. Cota, E. Pavón, M.C. Pazos, M.D. Alba, $Cs^{+}$ immobilization by designed micaceous adsorbent under subcritical conditions, Appl Clay Sci 143 (2017) 293–299, https://doi.org/10.1016/j.clay.2017.03.041.

[13] S. Komarneni, N. Kozai, W. Paulus, Superselective clay for radium uptake, Nature 410 (2001) 771.

[14] T. Yuan, S. Schymura, T. Bollermann, K. Molodtsov, P. Chekhonin, M. Schmidt, T. Stumpf, C. Fischer, Heterogeneous Sorption of Radionuclides Predicted by Crystal Surface Nanoroughness, Environ Sci Technol 55 (2021) 15797–15809, https://doi.org/10.1021/acs.est.1c04413.

[15] R. Martín-Rodríguez, F. Aguado, M.D. Alba, R. Valiente, A.C. Perdigón, Eu 3+ Luminescence in High Charge Mica: An in Situ Probe for the Encapsulation of Radioactive Waste in Geological Repositories, ACS Appl Mater Interfaces 11 (2019) 7559–7565. https://doi.org/Doi: 10.1021/acsami.8b20030.

[16] R. Martín-Rodríguez, R. Valiente, F. Aguado, A.C. Perdigón, Highly efficient photoluminescence from isolated $Eu^{3+}$ ions embedded in high-charge mica, J Mater Chem C Mater 5 (2017) 10360–10368, https://doi.org/10.1039/c7tc01818e.

[17] E. Pavón, M.A. Castro, M. Naranjo, M.M. Orta, M.C. Pazos, M.D. Alba, Hydration properties of synthetic high-charge micas saturated with different cations: An experimental approach, Am. Mineral. 98 (2013) 394–400, https://doi.org/10.2138/am.2013.4217.

[18] E. Pavón, M.A. Castro, A. Cota, F.J. Osuna, M.C. Pazos, M.D. Alba, Interaction of hydrated cations with mica-n (n = 2, 3 and 4) surface, J. Phys. Chem. C 118 (2014) 2115–2121, https://doi.org/10.1021/jp4110695.

[19] T. Kodama, M. Ueda, Y. Nakamuro, K.I. Shimizu, S. Komarneni, Ultrafine Na-4-mica: Uptake of alkali and alkaline earth metal cations by ion exchange, Langmuir 20 (2004) 4920–4925, https://doi.org/10.1021/la0362573.

[20] N.T. Skipper, P.A. Lock, J.O. Titiloye, J. Swenson, Z.A. Mirza, W.S. Howells, F. Fernandez-Alonso, The structure and dynamics of 2-dimensional fluids in swelling clays, Chem Geol 230 (2006) 182–196, https://doi.org/10.1016/j.chemgeo.2006.02.023.

[21] G. Sposito, N.T. Skipper, R. Sutton, S.H. Park, A.K. Soper, J.A. Greathouse, Surface geochemistry of the clay minerals, Proc Natl Acad Sci U S A 96 (1999) 3358–3364, https://doi.org/10.1073/pnas.96.7.3358.

[22] A.C. Perdigón, F. González, C. Pesquera, D. Li, C. Blanco, Novel acidic solids from high charge Na-micas by mild hydrothermal treatment, Microporous Mesoporous Mater. 133 (2010) 100–105, https://doi.org/10.1016/j.micromeso.2010.04.020.

[23] R. Ravella, S. Komarneni, C.E. Martinez, Highly charged swelling mica-type clays for selective Cu exchange, Environ Sci Technol 42 (2008) 113–118, https://doi.org/10.1021/es802507e.

[24] S. Diaz-Moreno, M. Amboage, M. Basham, R. Boada, N.E. Bricknell, G. Cibin, T. M. Cobb, J. Filik, A. Freeman, K. Geraki, D. Gianolio, S. Hayama, K. Ignatyev, L. Keenan, I. Mikulska, J.F.W. Mosselmans, J.J. Mudd, S.A. Parry, The Spectroscopy Village at Diamond Light Source, J Synchrotron Radiat 25 (2018) 998–1009, https://doi.org/10.1107/S1600577518006173.

[25] B. Ravel, M. Newville, ATHENA, ARTEMIS, HEPHAESTUS: data analysis for X-ray absorption spectroscopy using IFEFFIT, Urn:Issn:0909-0495 12 (2005) 537–541. Doi: 10.1107/S0909049505012719.

[26] A.C. Perdigón, D. Li, C. Pesquera, F. González, B. Ortiz, F. Aguado, C. Blanco, Synthesis of porous clay heterostructures from high charge mica-type aluminosilicates, J Mater Chem A Mater 1 (2013) 1213–1219, https://doi.org/10.1039/c2ta00543c.

[27] H. Kalo, W. Milius, M. Bräu, J. Breu, Synthesis and single crystal structure refinement of the one-layer hydrate of sodium brittle mica, J Solid State Chem 198 (2013) 57–64, https://doi.org/10.1016/j.jssc.2012.09.026.

[28] E.J.M. Hensen, T.J. Tambach, A. Bliek, B. Smit, Adsorption isotherms of water in Li-, Na-, and K-montmorillonite by molecular simulation, J. Chem. Phys. 115 (2001) 3322–3329, https://doi.org/10.1063/1.1386436.

[29] M. Chávez-Páez, L. DePablo, J.J. DePablo, Monte Carlo simulations of Ca-montmorillonite hydrates, J. Chem. Phys. 114 (2001) 10948–10953, https://doi.org/10.1063/1.1374536.

[30] R.D. Shannon, Revised effective ionic radii and systematic studies of interatomic distances in halides and chalcogenides, Acta Crystallographica A 32 (1976) 751–767. https://doi.org/Doi: 10.1107/S0567739476001551.

[31] F. Martelli, S. Abadie, J.P. Simonin, R. Vuilleumier, R. Spezia, Lanthanoids(III) and actinoids(III) in water: Diffusion coefficients and hydration enthalpies from polarizable molecular dynamics simulations, Pure Appl. Chem. 85 (2013) 237–246, https://doi.org/10.1351/PAC-CON-12-02-08.

[32] M.D. Alba, A.I. Becerro, M.A. Castro, A.C. Perdigón, Hydrothermal reactivity of Lu-saturated smectites: Part I, A Long-Range Order Study, American Mineralogist 86 (2001) 115–123, https://doi.org/10.2138/am-2001-0113.

[33] G. Brindley G.W., Brown, Crystal structures of Clay Minerals and their X-ray identification, Mineral Society, London, 1980.

[34] M.F. Brigatti, S. Guggenheim, Mica crystal chemistry and the influence of pressure, temperature, and solid solution on atomistic models, Rev Mineral Geochem 46 (2002) 1–97, https://doi.org/10.2138/rmg.2002.46.01.

[35] R.M. Hazen, L.W. Finger, D. Velde, Crystal structure of a silica and alkali rich trioctahedral mica, Am. Mineral. 66 (1981) 586–591.

[36] K. Binnemans, Interpretation of europium (III) spectra, Coord Chem Rev 295 (2015) 1–45, https://doi.org/10.1016/j.ccr.2015.02.015.

[37] G.S. Ofelt, Structure of the $f^6$ configuration with application to rare-earth ions, J Chem Phys 38 (1963) 2171–2180, https://doi.org/10.1063/1.1733947.

[38] G. Plancque, V. Moulin, P. Toulhoat, C. Moulin, Europium speciation by time-resolved laser-induced fluorescence, Anal Chim Acta 478 (2003) 11–22, https://doi.org/10.1016/S0003-2670(02)01486-1.

[39] M. Atanassova, V. Kurteva, I. Billard, Coordination chemistry of europium(III) ion towards acylpyrazolone ligands, Anal. Sci. 31 (2015) 917–922, https://doi.org/10.2116/analsci.31.917.

[40] N. Finck, M.L. Schlegel, A. Bauer, Structural iron in dioctahedral and trioctahedral smectites: a polarized XAS study, Phys Chem Miner 42 (2015) 847–859, https://doi.org/10.1007/s00269-015-0768-3.

[41] N. Finck, M. Bouby, K. Dardenne, T. Yokosawa, Yttrium co-precipitation with smectite: A polarized XAS and AsFlFFF study, Appl Clay Sci 137 (2017) 11–21, https://doi.org/10.1016/j.clay.2016.11.029.

[42] N. Finck, M.L. Schlegel, D. Bosbach, Sites of Lu(III) sorbed to and coprecipitated with hectorite, Environ Sci Technol 43 (2009) 8807–8812, https://doi.org/10.1021/es901940v.

[43] B.C. Bostick, M.A. Vairavamurthy, K.G. Karthikeyan, J. Chorover, Cesium adsorption on clay minerals: An EXAFS spectroscopic investigation, Environ Sci Technol 36 (2002) 2670–2676, https://doi.org/10.1021/es0156892.

[44] G.O. Lepore, E. Schingaro, E. Mesto, M. Lacalamita, C. Cristiani, P.G. Stampino, G. Dotelli, E. Finocchio, F. d'Acapito, G. Giuli, Lanthanum captured in montmorillonite: Evidence of inner-sphere complexes from X-ray Absorption Spectroscopy investigations, Appl Clay Sci 230 (2022) 106676, https://doi.org/10.1016/j.clay.2022.106676.

[45] A.J. Fuller, S. Shaw, M.B. Ward, S.J. Haigh, J.F.W. Mosselmans, C.L. Peacock, S. Stackhouse, A.J. Dent, D. Trivedi, I.T. Burke, Caesium incorporation and

retention in illite interlayers, Appl Clay Sci 108 (2015) 128–134, https://doi.org/10.1016/j.clay.2015.02.008.
[46] M.L. Schlegel, Polarized EXAFS characterization of the sorption mechanism of yttrium on hectorite, Radiochim Acta 96 (2008) 667–672, https://doi.org/10.1524/ract.2008.1551.
[47] M.L. Schlegel, M. Descostes, Uranium uptake by hectorite and montmorillonite: A solution chemistry and polarized EXAFS study, Environ Sci Technol 43 (2009) 8593–8598, https://doi.org/10.1021/es902001k.